Joule

CellPress

Article

Supramolecular design principles in pseudohalides for high-performance perovskite solar mini modules

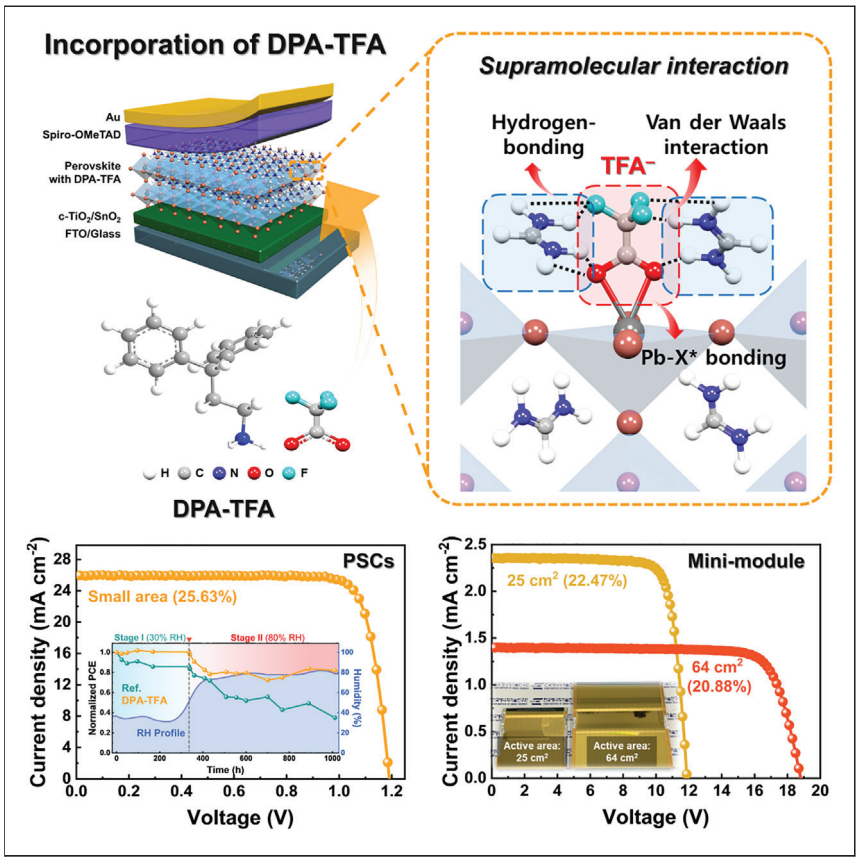

One of the critical issues in perovskite solar cells (PSCs) is the open-circuit voltage (V_{OC}) deficit due to surface or grain boundary defects. A dual-ion passivation strategy using TFA^- and DPA^+ achieved supramolecular passivation, resulting in a power conversion efficiency (PCE) of 25.63% and a V_{OC} of 1.191 V. Large-area modules also showed high performance, with 22.47% and 20.88% PCE for 25 and 64 cm^2, respectively. This highlights the importance of non-covalent interactions of pseudohalides in enhancing the efficiency and stability of PSCs.

Hochan Song, Hak-Beom Kim, Seong Chan Cho, ..., Sang Uck Lee, Yimhyun Jo, Hyosung Choi

minjae@kunsan.ac.kr (M.L.)
suleechem@skku.edu (S.U.L.)
yimhyun.jo@kier.re.kr (Y.J.)
hschoi202@hanyang.ac.kr (H.C.)

Highlights

The pseudohalide TFA^- effectively passivates perovskite via non-covalent interactions

DPA-TFA can suppress non-radiative recombination and local inhomogeneities

The small-area perovskite solar cells achieve a PCE of 25.63% with a V_{OC} of 1.191 V

The mini modules with areas of 64 cm^2 achieve a PCE of 20.88%

Song et al., Joule 8, 2283–2303
August 21, 2024
https://doi.org/10.1016/j.joule.2024.05.019

Joule

CellPress

Article

Supramolecular design principles in pseudohalides for high-performance perovskite solar mini modules

Hochan Song,[1,12] Hak-Beom Kim,[2,12] Seong Chan Cho,[3] Jeongjae Lee,[4] Jonghee Yang,[5] Woo Hyeon Jeong,[6] Ji Yeon Won,[1] Hong In Jeong,[1] Jiwoo Yeop,[7] Jin Young Kim,[7,8] Benjamin J. Lawrie,[9] Mahshid Ahmadi,[10] Bo Ram Lee,[6] Minjin Kim,[2] Seung Ju Choi,[2] Dong Suk Kim,[7,8] Minjae Lee,[11,*] Sang Uck Lee,[3,*] Yimhyun Jo,[2,*] and Hyosung Choi[1,13,*]

SUMMARY

In this work, we reveal the role of non-covalent interactions, which are known to play important roles in supramolecular phenomena, in achieving efficient perovskite surface and grain boundary passivation. By using a series of pseudohalides, we find that trifluoroacetate (TFA^-) provides the strongest binding to iodide vacancies by means of non-covalent hydrogen bonding and dispersion interactions. By exploiting additional non-covalent dispersion and hydrophobic interactions in aromatic 3,3-diphenylpropylammonium (DPA^+), we present a dual-ion passivation strategy that not only minimizes the non-radiative recombination center and local chemical inhomogeneities but also induces preferentially oriented growth of α-$FAPbI_3$ lattice. This leads to an outstanding power conversion efficiency (PCE) of 25.63% with an exceptional open-circuit voltage of 1.191 V in a perovskite solar cell with a small area, while perovskite solar mini modules with aperture areas of 25 and 64 cm^2 achieved PCE of 22.47% (quasi-steady-state [QSS]-certified 20.50%) and 20.88%, respectively, with outstanding stability under high-humidity conditions.

INTRODUCTION

Since the seminal report in 2009, organic-inorganic hybrid perovskites have witnessed remarkable advancements for solar cell applications owing to their outstanding optoelectronic properties and prospects for low-cost device fabrication via solution processing.[1,2] In particular, formamidinium (FA)-based lead triiodide ($FAPbI_3$) perovskite, with a narrow band gap of about 1.5 eV, is suitable for single-junction solar cells with improved thermal stability than the prototypic methylammonium (MA) counterpart,[3–5] making them the current leading materials for high-performance perovskite solar cells (PSCs) with a champion power conversion efficiency (PCE) of 26.08%.[6]

Notwithstanding the achievements, significant rooms for further improvements exist in terms of the PCEs of PSCs, considering the fundamental Shockley-Queisser limit of 31% for this band gap[7]; they also lag behind those of silicon solar cells (highest PCE record at 26.7%).[8] One of the main challenges in improving this efficiency lies in cutting the deficit in open-circuit voltage (V_{OC}). V_{OC} loss can stem from various factors, such as extended defects and charge transport layers, but one of the primary contributors is crystalline point defects such as antisites, interstitials, and halide vacancies.[9–12] Notably, substantial amounts of such defects are known to form in the

CONTEXT & SCALE

Formamidinium (FA)-based lead triiodide ($FAPbI_3$) perovskites have attracted great attention owing to their outstanding optoelectronic properties. Despite the achievements, perovskite solar cells (PSCs) still lag behind silicon solar cells. One of the main challenges in improving the efficiency of PSCs lies in cutting the deficit in open-circuit voltage (V_{OC}), primarily caused by crystalline point defects such as iodide vacancies (V_I).

Herein, by using pseudohalide as our proof of concept, we shed light on the role of non-covalent interaction and control defects on perovskite crystallite surfaces through a strategy we termed *supramolecular passivation*. As a result, PSCs with this strategy offer outstanding efficiency and stability in both small-area PSCs and large-area perovskite mini modules. Our work unveils the neglected role of non-covalent interactions for perovskite surface defect and grain boundary passivation, essential for designing effective additives toward efficient and stable PSCs.

polycrystalline perovskite structure—particularly at the surface and grain boundaries—as a result of solution processing.[11] These defects not only dissipate substantial photogenerated charge carriers via non-radiative recombination but also compromise the crystallinity and chemical homogeneity (i.e., via halide segregation) in the perovskite matrix, significantly curtailing the optoelectronic performances, including the V_{OC} deficit and carrier transport ability.[13–15] Thus, developing effective strategies to comprehensively regulate the perovskite defects and thereby minimize the non-radiative recombination center to mitigate carrier loss is imperative to provide a breakthrough by unlocking the full potential of PSCs.

Iodide vacancies (V_I), which are known to be abundant in the surface and grain boundaries of perovskite films due to their relatively low formation energies, are one of the most problematic among such defects: they not only leave uncoordinated Pb^{2+} as an additional defect species but also cause dynamic degradation of the matrices and optoelectronic performances and stability due to their mobile nature.[16–18] Given the anionic nature of the halides, straightforward filling and passivation of V_I can be expected with various types of small molecular anions,[19–22] which are commonly called pseudohalides due to their similarities in size, but with extra opportunities for forming stronger bonds due to their asymmetric molecular structure bestowing dipole moment-based bonds such as hydrogen bonds.[20,23–27] For instance, a state-of-the-art PSC with an outstanding performance of 25.6% has been successfully demonstrated by manifesting comprehensive defect passivation and improved perovskite crystallinity upon formate ($HCOO^-$) incorporation.[28]

Although extensive investigations on V_I passivation based on pseudohalides and other larger organic/inorganic passivating agents have been reported to date,[20] the attention was mostly paid on the nature of terminal anchoring groups in determining the binding ability of passivating agents toward the defects. By contrast, the effect of (presumably non-trivial) non-covalent interaction, often between the functional groups within the rest of passivating species and the neighboring perovskite scaffold (i.e., Pb–I sublattice), not to mention the additional synergistic effect between these species and other functional ligands on the perovskite surface, has been left relatively unexplored.[29,30]

Herein, by using pseudohalide as a model system, we shed light on the role of non-covalent interaction in controlling efficient passivation of perovskite crystallite surfaces. It is shown that the binding energy of pseudohalides to the perovskite surface is governed not only by the bonding action of terminal anchoring group toward the V_I defects but also by non-covalent interactions with surrounding FA and Pb–I sublattice through non-covalent interactions, which are known to be important for controlling supramolecular phenomena.[31,32] We explicitly screen the possible pseudohalide molecular landscape with *ab initio* methods, which identify trifluoroacetate (TFA^-) anion as the pseudohalide candidate with the largest effective molecular volume interacting with the perovskite sublattice. Furthermore, we extend this concept of supramolecular non-covalent interaction to cation passivating agents as well to achieve a dual-ion passivation strategy: we employ 3,3-diphenylpropylammonium (DPA^+), a molecule with two phenyl rings which has previously been proven to provide strong dispersion and hydrophobic interactions.[33] Thus, we achieve *a supramolecular passivation of α-$FAPbI_3$ perovskite lattice* by incorporating both ions into the precursor solution. We term this DPA-TFA passivation, by which a surface defect-passivated lattice with a preferred orientation along the vertical direction, greatly mediating the local phase and chemical inhomogeneities. Such features collectively

[1]Department of Chemistry, Research Institute for Convergence of Basic Science and Research Institute for Natural Sciences, Hanyang University, Seoul 04763, Republic of Korea

[2]Ulsan Advanced Energy Technology R&D Center, Korea Institute of Energy Research, Ulsan 44776, Republic of Korea

[3]School of Chemical Engineering, Sungkyunkwan University (SKKU), Suwon 16149, Republic of Korea

[4]School of Earth and Environmental Sciences, Seoul National University, Seoul 08826, Republic of Korea

[5]Department of Chemistry, Yonsei University, Seoul 03722, Republic of Korea

[6]School of Advanced Materials Science and Engineering, Sungkyunkwan University (SKKU), Suwon 16149, Republic of Korea

[7]School of Energy and Chemical Engineering, Ulsan National Institute of Science and Technology (UNIST), Ulsan 44919, Republic of Korea

[8]Graduate School of Carbon Neutrality, Ulsan National Institute of Science and Technology (UNIST), Ulsan 44919, Republic of Korea

[9]Center for Nanophase Materials Sciences and Materials Science and Technology Division, Oak Ridge National Laboratory, Oak Ridge, TN 377831, USA

[10]Institute for Advanced Materials and Manufacturing, Department of Materials Science and Engineering, University of Tennessee, Knoxville, TN 37996, USA

[11]Department of Chemistry, Kunsan National University, Gunsan 54150, Republic of Korea

[12]These authors contributed equally

[13]Lead contact

*Correspondence: minjae@kunsan.ac.kr (M.L.), suleechem@skku.edu (S.U.L.), yimhyun.jo@kier.re.kr (Y.J.), hschoi202@hanyang.ac.kr (H.C.)

https://doi.org/10.1016/j.joule.2024.05.019

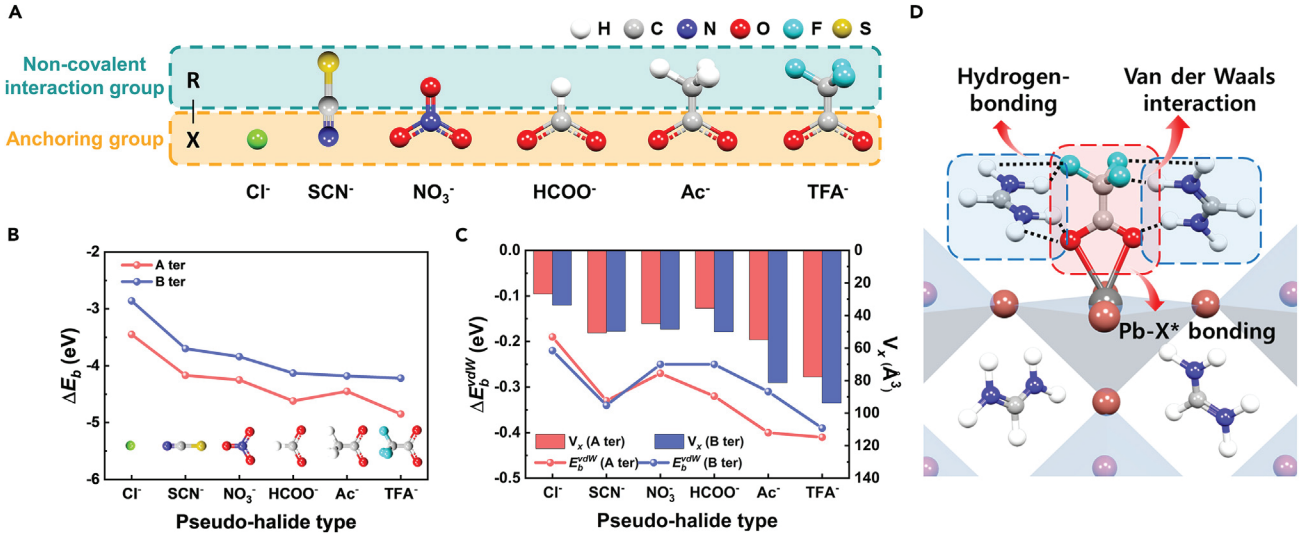

Figure 1. DFT calculations predict non-covalent interactions between pseudohalides and perovskite

(A) The pseudohalide structures with two groups: a non-covalent interaction group (R) and an anchoring group (X).

(B) The binding energies (ΔE_b) of X* depend on A and B terminations.

(C) Non-covalent interactions with the relationship between van der Waals interaction (ΔE_b^{vdW}) and the effective volume (V_x) of X* on the $FAPbI_3$ surface.

(D) Schematic illustration of non-covalent interactions of TFA^- on the $FAPbI_3$ surface, hydrogen bonding, and van der Waals interaction.

offer efficient charge transport pathway while minimizing non-radiative recombination, benefiting the optoelectronic performance of the perovskite film.

As a result, PSCs with a supramolecular-passivated perovskite matrix offer an outstanding PCE of 25.63% as well as impressive V_{OC} of 1.191 V, along with PCE of 22.47% (quasi-steady-state [QSS]-certified PCE of 20.50%) and 20.88% in large-area PSC mini modules with a respective aperture area of 25 and 64 cm^2. Furthermore, the supramolecular-passivated PSCs exhibited outstanding shelf-life stability, maintaining 92% of the initial efficiency for 10,000 h. Even under high-humidity conditions, these PSCs showed remarkable efficiency with 82% of the initial efficiency remaining after 1,000 h. Our work unveils the hitherto neglected role of supramolecular non-covalent interactions for perovskite surface defect and grain boundary passivation and renders key chemical principles necessary for designing effective molecular additives toward the realization of high-performance PSCs.

RESULTS

Energetic contribution of non-covalent interactions to surface binding of pseudohalides

By utilizing density functional theory (DFT) calculations, we first explored the coordinating action of the candidate pseudohalides to the stoichiometric defects V_I through the anionic functional group (i.e., anchoring group) and non-covalent interactions between the end groups and the neighboring perovskite scaffold in the vacancy pocket (i.e., non-covalent interaction group). Chloride (Cl^-) and five different pseudohalides—nitrate (NO_3^-), thiocyanate (SCN^-), formate ($HCOO^-$), acetate (Ac^-), and TFA^-—were selected as candidates (denoted as X*), and their binding energies onto V_I pocket in $FAPbI_3$-based perovskites were calculated (Figure 1A), based on the observations that X* preferentially resides on the perovskite crystallite surface (Figure S1; Table S1). We then calculated the binding energies (ΔE_b) of X* on the V_I at $FAPbI_3$ surface (Figures S2 and S3). Irrespective of FA iodide (FAI)- or PbI_2-exposed

surface (A and B terminations, respectively), all selected species exhibited negative ΔE_b values, indicating that binding to the perovskite surface was thermodynamically preferred for all X* (Figure 1B). The calculated binding energies monotonically increase with the following trend: Cl^- < SCN^- < NO_3^- < carboxylates ($HCOO^-$ < Ac^- < TFA^-). We note that although values of ΔE_b are principally determined by the chemical nature (i.e., functional group) of the X* species on the order of ~eV, subtle differences in ΔE_b also exist across the three carboxylate-based X* ($HCOO^-$, Ac^-, and TFA^-). This strongly suggests that non-covalent interactions such as dispersion (van der Waals) forces, steric effects, and hydrogen bonding, which all involve the non-covalent moieties of the pseudohalide and the perovskite scaffold upon its coordination, also play a non-negligible role in the binding action of X* toward V_I (Figure S4).

To ascertain this hypothesis, we conducted crystal orbital Hamilton population (COHP) analysis to separately evaluate the contribution of non-covalent interactions and the covalent bonding between pseudohalides and Pb^{2+} on the surface of $FAPbI_3$ (Figure S5). The calculated "integrated COHP" value showed similar positive values for all pseudohalides, while TFA^- showed the smallest value. This demonstrates that the strong binding energy of TFA^- is largely contributed by non-covalent interaction. Furthermore, we examined the relationship between the effective volume (V_X) of the three carboxylate-based X*s and binding energy by van der Waals interaction (ΔE_b^{vdW}), which should be proportional to the size of electron clouds in the X* and thus should scale with V_X. The corresponding data in Figure 1C and Table S2 confirm this hypothesis: ΔE_b^{vdW} scales approximately linearly with V_X. As V_X of pseudohalide increases, the expanded X* can interact more effectively with the neighboring FA^+ and Pb-I through van der Waals interaction. This trend is not only limited to the carboxylate anions but applies equally well to other X* candidates such as Cl^-, SCN^-, and NO_3^-. Furthermore, as shown in Figure 1D, TFA^- stands out here with the largest V_X that can exhibit stronger interactions than other candidates. Additionally, the presence of highly electronegative fluorine atoms in the $-CF_3$ group suggests a feasibility of hydrogen bonding with the protons in neighboring FA^+, culminating in stronger non-covalent interactions, as shown in the final relaxed surface structures (Figure S6). These results collectively suggest that the TFA^- can establish the strongest non-covalent interactions with the perovskite sublattice, enabling to construct supramolecular-passivated perovskite matrix with a more complete surface defect passivation.

For the choice of cation, we further exploit the theme of supramolecular interaction in binding and functionalities of passivating agents to ameliorate the problem of phase transition in $FAPbI_3$ perovskites by reaction with moisture (*vide infra*). Moisture protection would require molecules with strong hydrophobic interaction as well as strong binding afforded by dispersion interaction, making aromatic molecules the best candidate for this functionality: we previously reported that the incorporation of DPA^+, a cation with two phenyl rings, to perovskite nanocrystals simultaneously enhances the electrical conductivity across the perovskite surface as well as bestows more stable environmental durability by blocking action of bulky phenyl groups toward moisture penetration.[33] We also note that the $-CF_3$ group in TFA^- may also open up possibilities for additional supramolecular non-covalent interactions involving fluorine, such as fluorine-π interactions (attractive interactions between the aromatic π electron cloud and electronegative fluorine atom), hydrogen bonding to aromatic C–H moieties, and extra dispersion interactions, which could be exploited to strengthen the binding of unsaturated aromatic molecules to perovskite surfaces.[34–36]

Thus, taken collectively, we predict that DPA-TFA passivation would bestow several favorable properties to the perovskite surface: (1) efficient surface passivation for V_I through tightly bound DPA^+ and TFA^- by means of strong dispersion interaction between the molecules and the perovskite lattice; (2) possible synergistic binding of both molecules by intermolecular interactions among DPA^+ and TFA^-; and (3) enhanced phase stability by blocking moisture penetration through hydrophobic interactions.

Atomistic-scale surface binding mechanism of DPA-TFA

Based on the above computational prediction and concepts in supramolecular interactions, we focused on the optimization of $FAPbI_3$ perovskite film formation by incorporating DPA-TFA into the precursor solution. Probing the proposed supramolecular non-covalent interactions in perovskite films is, however, not straightforward due to the relatively low concentration and absence of long-range periodicity in arrangement of these molecular species relative to the perovskite bulk. In addition, finding spectroscopic evidence for such interaction requires techniques capable of probing the interatomic proximities; hence, we opted for solid-state nuclear magnetic resonance (NMR) experiments to verify their existence.

Figure 2A shows the ^{19}F direct excitation solid-state NMR spectra of pristine DPA-TFA salt, which shows a single broadened peak at −82.1 ppm. Since there are no other fluorine environments in this system, this peak must arise from the trifluoro (–CF_3) functional group in TFA^-, where the broadening presumably arises from poorly averaged strong ^1H-^{19}F and ^{19}F-^{19}F dipolar coupling in the DPA-TFA salt, a result of using a relatively slow magic-angle spinning frequency of 10 kHz (no external ^1H decoupling was applied during acquisition). When this DPA-TFA salt is added to the perovskite film, a new sharp ^{19}F peak appears at −81.5 ppm, which is ascribed to the perovskite-bound TFA^-; a clear narrowing of the peak, in this case, is likely an effect of TFA salts being separated from the DPA cations by binding to the perovskite surface, contrary to the case in the pristine salt.

Further evidence of this passivation, as well as intermolecular interactions involving DPA-TFA, can be found via ^{13}C cross-polarization (CP) experiments. Briefly, these experiments allow selective detection of ^{13}C species in spatial proximity to either ^1H (^1H-^{13}C CP) or ^{19}F (^{19}F-^{13}C CP). Since these experiments rely on dipolar coupling, which does not require electron sharing (as in *J*-coupling), signals from ^{13}C species both covalently and non-covalently bonded to ^1H/^{19}F are detected on these spectra. Figure 2B shows the ^1H-^{13}C CP spectra of pristine $FAPbI_3$, DPA-TFA salt, and DPA-TFA passivated $FAPbI_3$, with the spectra labeled in color scheme matching the atomic positions in the molecule in Figure 2A. As expected, the passivated sample shows signal coming from FA as well as DPA^+ (i.e., molecules with ^{13}C covalently bonded to ^1H); at the same time, however, it shows a ^{13}C signal at 162 ppm matching with that of TFA^- carbonyl signal. Since there are no protons in TFA^-, this peak signifies that TFA^- molecules are in close proximity to proton-containing molecules, which in this case must be either FA^+ or DPA^+, thus confirming the existence of supramolecular interactions in the system.

Further evidence for this interaction is also found by examining the ^{19}F-^{13}C CP, which provides an alternative window through which this interaction can be probed. Figure 2C shows the ^{19}F-^{13}C CP spectra of pristine $FAPbI_3$, DPA-TFA salt, and DPA-TFA passivated $FAPbI_3$, with the spectra again labeled in color scheme consistent with that of Figure 2A. Note that the $FAPbI_3$ spectrum was obtained with ^1H-^{13}C CP (same to (B)) and is provided as a reference only. As expected, the spectrum of

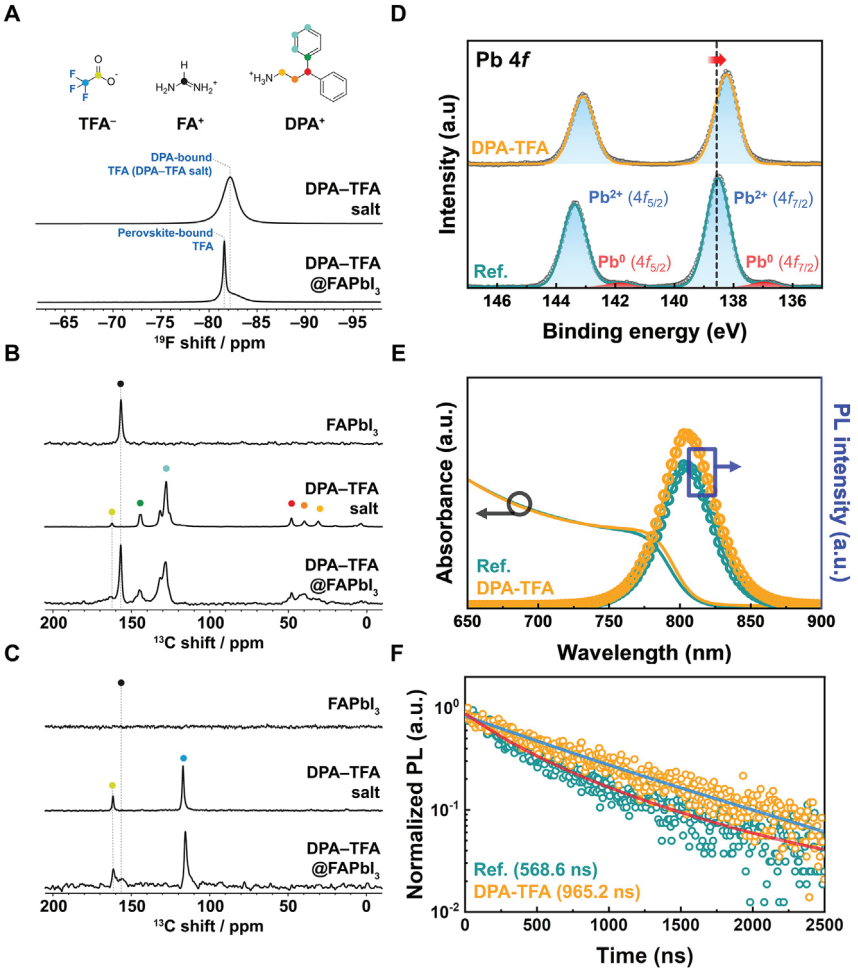

Figure 2. Identification of non-covalent interaction between DPA-TFA and perovskite realizing comprehensive surface defect passivation

(A–C) Solid-state NMR spectra of DPA-TFA film, measured with (A) ^{19}F direct excitation, (B) ^{1}H-^{13}C CP (^{1}H decoupled), and (C) ^{19}F-^{13}C CP (^{19}F decoupled). NB: the $FAPbI_3$ spectrum was obtained with ^{1}H–^{13}C CP (same to B) and is provided as a reference. Peaks are labeled with color scheme consistent with shown in (A).

(D) XPS Pb 4*f* core-level spectra of the reference and DPA-TFA perovskite film.

(E) The absorption spectra and steady-state PL spectra of the reference and DPA-TFA perovskite film.

(F) Time-resolved PL decay of the reference and DPA-TFA perovskite film.

DPA-TFA salt is of little significance as it only shows the TFA^- peaks. However, the passivated $FAPbI_3$ sample clearly shows FA^+ signal at 156 ppm, *even though* FA^+ *does not contain any fluorine atoms*. Considering the selectivity of ^{19}F-^{13}C CP, this means that the FA^+ molecules are in a close proximity—presumably via a non-covalent interaction—to TFA^- molecules, which are the only species containing ^{19}F. Regarding the possible cooperative binding of TFA and DPA molecules (*vide supra*), we note that the aromatic DPA peaks are absent in ^{19}F-^{13}C CP spectrum; this likely arises from inability to decouple on ^{1}H and ^{19}F channels simultaneously due to limitations in our NMR probe, significantly broadening the DPA peaks to render them unobservable. Thus, although further experimental efforts are required to clarify and fully elucidate the nature of this supramolecular cooperative binding by use of advanced NMR spectroscopic methods, our ^{19}F-^{13}C CP data provide an

unambiguous evidence of supramolecular non-covalent interaction between FA^+ and TFA^-, in agreement with the computational predictions above.

In addition, X-ray photoelectron spectroscopy (XPS) measurements were conducted to explore how the chemical structure of the perovskite films is affected by the introduction of DPA-TFA. A ~0.3 eV downshift of binding energy as well as the suppression of metallic Pb^0 peak were observed in Pb 4*f* core-level XPS spectra upon DPA-TFA incorporation (Figure 2D). Given the weaker covalent bond strength of Pb-TFA than Pb-I, it is likely that the electron density of the Pb^{2+} is increased upon TFA coordination, resulting in the observed downshift. Concurrently, the high electron density of CF_3 in TFA^-, as well as its large effective volume upon filling the V_I, can increase partial electron density of the neighboring I^- and FA^+ in the perovskite lattice scaffold and/or uncoordinated Pb species at the perovskite surface.[21,37] This supramolecular interaction can lead to the increased electron densities in I and N elements in the TFA-coordinated perovskite, which is corroborated by the concurrent spectral downshift in I 3*d* and N 1*s* core-level XPS spectra (Figure S7). The reduction of PbI_2 species—known to undergo photolysis by X-ray beam during XPS experiments[38–40]—upon DPA-TFA incorporation could also be responsible for the disappearance of Pb^0 peaks. Overall, these results clearly support our hypothesis that DPA-TFA incorporation manifests comprehensive surface defect passivation via strong non-covalent interaction with perovskite lattice.

To study the influence of DPA-TFA on optical properties, we measured ultraviolet-visible (UV-vis) absorption and steady-state photoluminescence (PL) of the perovskite films (Figure 2E). At an optimal DPA-TFA concentration of 0.5% that does not notably compromise the perovskite grain sizes (Figure S8; Note S4), the absorption spectra showed a similar onset and optical band gap of 1.54 eV as confirmed by the Tauc plot (Figure S9), suggesting that the incorporation of DPA-TFA does not compromise the absorption range of the perovskite film. On the other hand, the DPA-TFA-incorporated film exhibited a 1.25-fold increase in PL intensity, indicating a reduction in non-radiative recombination center by surface defect passivation by DPA-TFA.[41] Time-resolved PL (TRPL) decay measurements were conducted to quantitatively compare charge recombination. The PL decay curves in Figure 2F were estimated via bi-exponential decays, consisting of a fast component (τ_1) and a slow component (τ_2). τ_1 represents the PL decay affected by carrier loss via non-radiative recombination induced by trap states formed due to the surface defects, while τ_2 represents the PL decay affected by free charge carriers.[42,43] The reference film showed τ_1 of 278.8 ns and τ_2 of 795.9 ns, while the DPA-TFA-incorporated film exhibited extended τ_1 of 625.6 ns and τ_2 of 1,292.9 ns (Table S3), corroborating our hypothesis that DPA-TFA effectively passivated defect sites on the surface of the perovskite crystallite and suppressed non-radiative recombination centers.[44]

Crystallographic properties upon DPA-TFA binding

It is known that the orientation of perovskite lattices is greatly influenced by the molecular interaction in the precursors during crystallization, which can also be manifested by the supramolecular lattice control with DPA-TFA.[37,45,46] We further implemented 2D grazing-incidence wide-angle X-ray scattering (GIWAXS) experiments to explore the crystallographic structures of the perovskite films. Two different incidence angles—0.1° and 0.5°—were utilized, allowing to further compare the crystallographic structures at the foremost surface (<5 nm) and the bulk of the perovskite films with different DPA-TFA concentrations, as, respectively, shown in Figures 3A, 3B, and S10.[47,48] At an incidence angle of 0.1°, the Debye-Scherrer rings at q = ~1.0 $Å^{-1}$ (corresponding to α-$FAPbI_3$ (100)) with different local contrasts in intensity

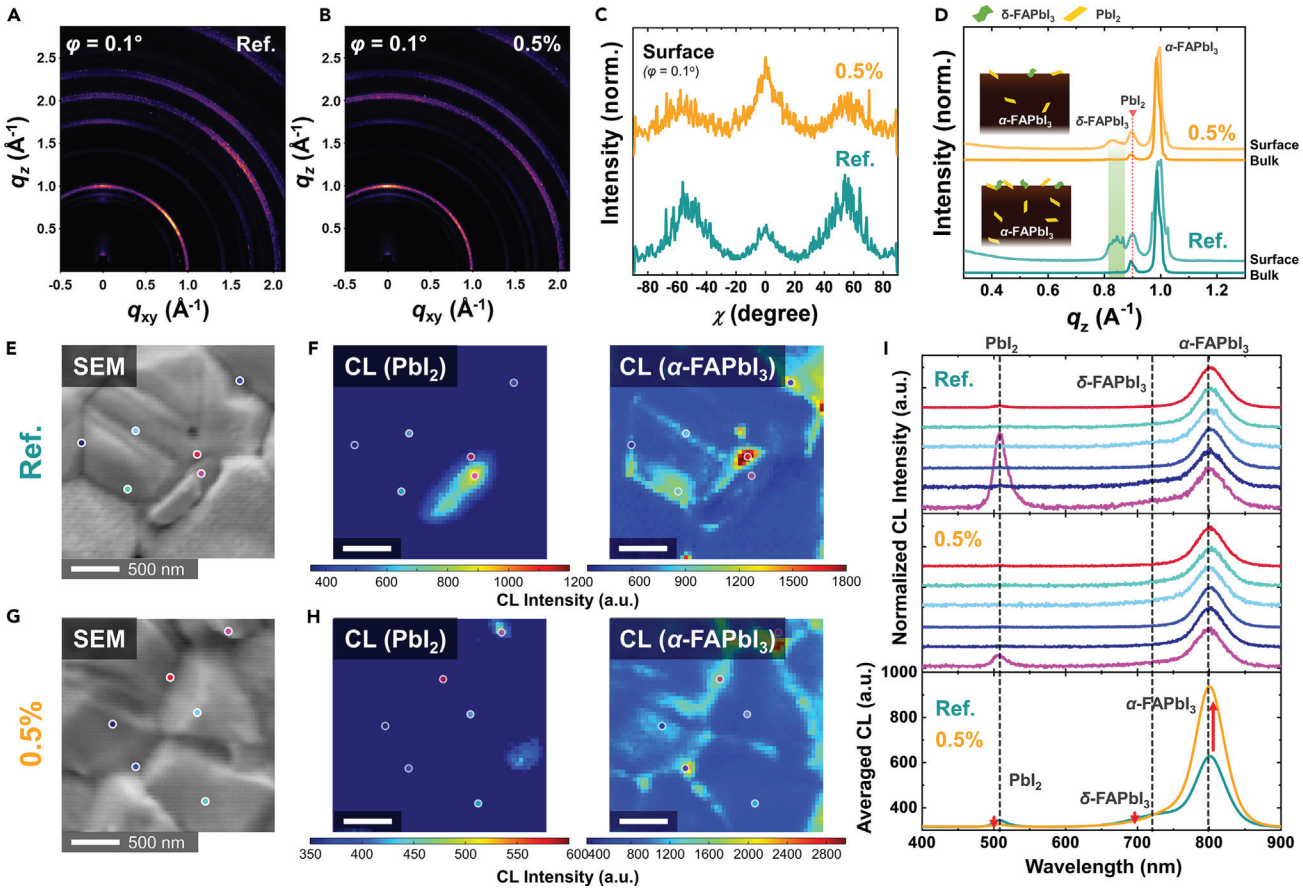

Figure 3. Supramolecular lattice passivation offers the preferred crystal orientation of perovskite matrix along the vertical direction while minimizing local phase and chemical inhomogeneities

(A and B) 2D GIWAXS patterns at an incident angle of 0.1° for (A) the reference and (B) 0.5 mol % DPA-TFA films.

(C) Azimuthally integrated GIWAXS intensity profiles of the perovskite films along the ring at $q \sim 1.0$ Å^{-1}, corresponding to the (100) facet of α-FAPbI$_3$, extracted from (A) and (B).

(D) Surface and bulk ($\varphi = 0.1°$ and 0.5°, respectively) q_z GIWAXS line-cut profiles of the reference and 0.5 mol % DPA-TFA films. Insets show respective populations and distributions of local impurity phases in the corresponding film.

(E–H) (E and G) SEM images and (F and H) PbI$_2$ ($\lambda = 508$ nm) and perovskite CL ($\lambda = 808$ nm) maps (1 nm bandwidth) for (E and F) reference and (G and H) DPA-TFA-incorporated films, respectively, collected by hyperspectral CL microscopy (scale bars, 500 nm).

(I) Local and averaged CL spectra for the corresponding perovskite films.

were observed in all cases, suggesting the perovskites exhibit preferential lattice orientations at the surface. Azimuthally integrated intensity profiles clearly reveal that DPA-TFA incorporation manifests preferentially oriented α-FAPbI$_3$ lattice along the vertical direction compared with the reference counterpart (Figure 3C). This is likely associated with the controlled crystallization of α-FAPbI$_3$ by bulky ammonium cations—here, DPA$^+$—that promotes the preferential growth of the perovskite lattice.[7] This can mitigate the emergence of defects at grain boundaries, thereby allowing efficient charge transport while minimizing recombination loss.

Additionally, two distinctive scattering signals at $q = 0.85$ and 0.9 Å^{-1}—assigned to be δ-FAPbI$_3$ and PbI$_2$, respectively—exclusively emerged along the q_z direction in the reference film. This indicates that these impurity phases emerged along the face-on orientation at the perovskite surface, which are detrimental to device performance and stability.[14,49] These signals become reduced with increasing DPA-TFA concentrations up to 2.0 mol %, as clearly visualized in the q_z-directional line-cut

profiles from the GIWAXS patterns of the corresponding films (Figures 3D and S11). This clearly shows that DPA-TFA also effectively mitigates such phase inhomogeneities, thereby rendering a high-quality perovskite film suited to device applications. Note that both the PbI_2 δ-$FAPbI_3$ signals become lower and negligible, respectively, in the bulk GIWAXS collected at 0.5° incidence angle. These observations suggest that such phase impurities mainly emerged at the top surface, highlighting the additional role of surface defect passivation that deters the emergence of local phase inhomogeneities compromising photovoltaic performances.[14,49]

The spectroscopic observations confirm that the supramolecular interaction by DPA-TFA incorporation renders a more complete surface defect passivation. The phase and chemical inhomogeneities—local distribution of vacancy defects—in the perovskite lattice are known to emerge and be aggravated by those defects.[14,50] Thus, these observations further hint that such inhomogeneities could be mitigated by the supramolecular interaction. We further explored the nanoscopic phase and chemical inhomogeneity in the perovskite matrices via hyperspectral cathodoluminescence (CL) microscopy.[14] For the reference film, intense 508 nm CL is observed from the ~500 nm-width crystallite at the perovskite surfaces shown in Figures 3E and 3F. This indicates that local PbI_2 impurities emerge at the perovskite surface, resulting in degraded optoelectronic performances and stability of the perovskite matrix.[14,49] Also, the uneven α-$FAPbI_3$ CL signal across the scanned area suggests that the perovskite grains are chemically inhomogeneous, rendering distinctive contrast in local defect densities, likely resulting in non-trivial energetic disorder at the perovskite surface that causes inhomogeneous local charge transport through the matrix.[14,51] By contrast, the DPA-TFA film exhibits not only a cleaner perovskite surface where the local PbI_2 CL is greatly suppressed but also lower CL contrast in α-$FAPbI_3$ grains (Figures 3G and 3H). This indicates that effective phase and chemical homogenization of the perovskite matrices are achieved upon DPA-TFA incorporation (statistical analysis of this homogenization is shown in Figure S12). Spectrally, we further observed a shoulder in the perovskite CL at ~710 nm that is likely associated with the construction of α/δ phase junction by the emerged δ-$FAPbI_3$,[52,53] which is largely suppressed upon DPA-TFA incorporation (Figure 3I). Overall, these observations clearly suggest that the supramolecular lattice control by DPA-TFA incorporation effectively homogenizes the chemical composition in the perovskite matrix while suppressing the emergence of the phase impurities—the latter consistent with GIWAXS results. This subsequently renders a smooth charge transport pathway, minimizing non-radiative recombination in both the perovskite matrix and perovskite/HTL interface, thereby boosting optoelectronic performances.[54,55] At a macroscopic perspective, we observed 2.28- and 2.34-fold enhancements in perovskite PL intensity for the half and full device stacks, respectively (Figure S13), further corroborating our hypothesis.

Device performance and characterization

To investigate photovoltaic performance of the supramolecular-passivated perovskite matrix, we fabricated the solar cell devices with n-i-p structure (Figure S14). Reference device without DPA-TFA in $FAPbI_3$ layer was also fabricated for comparison. Figures 4A and 4B show current density-voltage (*J-V*) curves and external quantum efficiency (EQE) spectra of the champion devices, respectively. The reference device exhibited a short-circuit current density (J_{SC}) of 25.75 mA cm^{-2}, V_{OC} of 1.166 V, fill factor (FF) of 80.79%, and PCE of 24.26%. By contrast, the device with DPA-TFA has a higher PCE of 25.63% (certified PCE 25.44%; Figure S15) with J_{SC} of 26.00 mA cm^{-2}, V_{OC} of 1.191 V, and FF of 82.77%. The integrated J_{SC} values from the EQE spectra for both the reference and DPA-TFA devices were found to

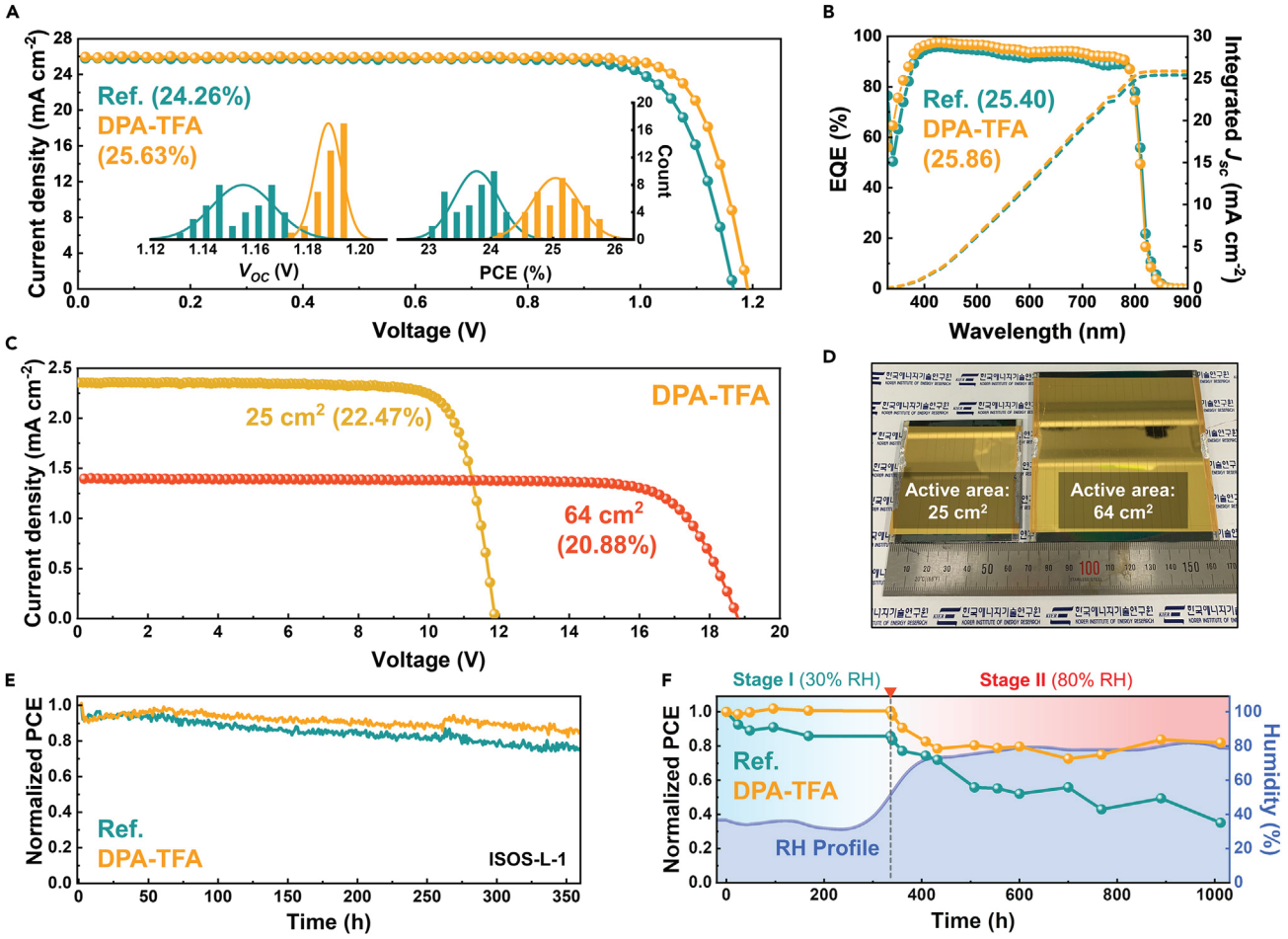

Figure 4. PSCs with supramolecular-passivation perovskite lattice manifest outstanding performances and stabilities

(A and B) (A) *J-V* curves (inset: statistical V_{OC} and PCE distribution, 40 devices for each device) and (B) EQE spectra (with integrated J_{SC}) of the reference and DPA-TFA PSCs.

(C and D) (C) *J-V* curves and (D) photographs image (viewed from the top electrode side) of the DPA-TFA PSC mini modules with an aperture area of 25 and 64 cm^2, respectively.

(E) MPP tracking for encapsulated devices under continuous one-sun illumination.

(F) Stability of PSCs under humid condition (intentionally increase the humidity up to 80%).

be in good agreement with the those from the *J-V* measurement (25.40 and 25.86 mA cm^{-2}, respectively; Figure 4B). The enhancements in both V_{OC} and FF are mainly responsible for the improved PCE of solar cells as a result of the exploitation of supramolecular lattice interactions through the non-covalent interaction of DPA-TFA, and comprehensive surface defect passivation, homogenized phase and chemical compositions, as well as preferentially vertical-oriented growth of α-$FAPbI_3$ lattice synergistically render a cleaner and smoother charge transport pathway with a minimized recombination loss. We observed a significant suppression of hysteresis behavior in DPA-TFA device with a calculated hysteresis index of 0.94% compared with that of the reference device (7.01%; Figure S16). This strongly suggests that the charge accumulation behaviors—associated with the internal defects and/or local phase impurities at grain boundaries and/or buried surface with charge transport layer—in device operation have been substantially mitigated by incorporating DPA-TFA.[14,49,56–58] This in turn highlights the powerfulness of DPA-TFA-based supramolecular passivation in regulation of local phase inhomogeneity, subsequently

establishing a better charge transport environment across the perovskite matrix that bestows excellent solar cell performances.[14,49,56–60]

We assessed the performances and reproducibility of the solar cells utilizing different (pseudo)halides, I^- and Ac^- (Figures S17 and S18). Both devices with DPA-I and DPA-Ac reproducibly rendered improved PCEs with nominal V_{OC} enhancements (1.177 and 1.174 V for DPA-I and DPA-Ac, respectively), which are lower than those of DPA-TFA-based devices. Additionally, to confirm the independent effect of TFA^-, we evaluated the device performance by incorporating FA-TFA (Figure S19). The device with FA-TFA showed improved efficiency, primarily due to a significantly increased V_{OC}. These observations further corroborate that the comprehensive surface binding action of TFA^-, which fully exploits its inherent non-covalent interaction capability as supramolecular interaction, is the primary factor in performance enhancements of PSCs; the incorporation of DPA-TFA substantially passivates the surface defects, thereby suppressing the non-radiative recombination and manifesting unprecedent V_{OC} improvements.

The effect of DPA-TFA concentration in the perovskite precursors (up to 2.0 mol %) on the device performance was explored (Figure S20). Gradual PCE increases—mainly attributed top V_{OC} and FF enhancements—were observed up to the DPA-TFA concentration of 0.5 mol %, which starts to drop with further increasing the concentration; the device with 2.0 mol % DPA-TFA plummeted to significantly low PCE of 15.88%. These observations strongly align with the hypothesis from the corresponding SEM images (Figure S8), where the increases of void densities and local phase inhomogeneities negate the functionalities of the DPA-TFA additive. At an optimal DPA-TFA concentration (0.5 mol %), operational stability of the encapsulated PSC was assessed by maximum power point (MPP) tracking (Figures 4E and S21), following the test protocols of the International Summit on Organic Photovoltaic Stability (ISOS-L-1).[61] The DPA-TFA device maintained 86% output from the initial PCE (22.62%) after 360 h of irradiation (at 263 h, the program was shut down and restarted immediately), while that of the reference device (21.95%) was reduced to 75%. These results also highlight the efficacy of supramolecular lattice passivation with DPA-TFA for demonstration of high performance and stable operation of PSCs, likely attributed to improved charge extraction and suppression of interfacial charge accumulation.

To understand how the comprehensive surface defect passivation realized by supramolecular lattice control upon DPA-TFA incorporation—evidenced by V_{OC} enhancements—practically affects the charge transport and recombination behaviors,[62] light intensity dependence of V_{OC} for the solar cell devices was explored (Figure S22). The ideality factor (n_{id}) of each device was deduced from the slope of the corresponding plot, providing insights into the charge recombination behaviors in devices under open-circuit conditions—as the value approaches two, the contribution of trap-assisted recombination becomes significant.[28] the n_{id} of the DPA-TFA device was calculated to be 1.078, showing a great suppression of trap-assisted recombination process compared with the reference device (corresponding n_{id} of 1.715) as a result of comprehensive surface defect passivation. The longer carrier lifetime in solar cell with DPA-TFA measured by transient photovoltage (TPV) experiments also corroborates this (Figure S23).[22,33] To quantify the trap densities in the perovskite films, space-charge-limited current (SCLC) behaviors (Figure S24) were analyzed. Indeed, the trap density of the DPA-TFA perovskite film is markedly lower (2.75×10^{15} cm^{-3}) than the reference counterpart (7.41×10^{15} cm^{-3}). Together, these observations clearly demonstrate the powerfulness of exploiting the supramolecular interaction

on perovskite surface defect passivation, which is deemed to be achieved by the substantial non-covalent interactions of TFA^- with perovskite lattice.[20,22]

The phase and chemical homogenization effect through comprehensive surface passivation action of DPA-TFA indeed realizes excellent small-area PSC performances, which also benefits in demonstrating high-performance large-area PSC mini module, a genuine goal of PSC toward ubiquitous realization. Figures 4C and 4D show *J-V* curves and photographs for the DPA-TFA PSC mini module with an aperture area of 25 and 64 cm^2, achieving PCE of 22.47% and 20.88%, respectively (details in Figure S25; Table S4). In comparison, reference PSC mini modules with the same aperture areas demonstrated lower performance, with PCEs of 20.12% and 18.60% for an aperture area of 25 and 64 cm^2 mini modules, respectively (Figure S26). For the certification of the DPA-TFA PSC mini module, we entrusted the certification to an independent laboratory (OMA Company, Korea) and obtained efficiencies of 22.21% and 20.86% for an aperture area of 25 and 64 cm^2, respectively (Figures S27 and S28). Moreover, DPA-TFA PSC mini module with an aperture area of 25 cm^2 achieved a PCE certification of 20.50% through QSS current-voltage (QSS-IV) measurements conducted by the National Renewable Energy Laboratory (NREL) and Newport (Figures S29 and S30). These results stand as one of the best performances among PSC mini modules (Figure S31; Table S5). These achievements strongly suggest that the supramolecular lattice passivation with DPA-TFA effectively manifests phase and chemical homogenization in the perovskite matrix across the large area, thereby realizing the scalable production of efficient PSC modules.

Stability of perovskite films and devices under ambient and humid conditions

Perovskite suffers from rapid phase transition to the photo-inactive δ-$FAPbI_3$ phase under ambient conditions—particularly moisture, where the presence of surface defects significantly accelerates this degradation.[63,64] Therefore, regulating the density of the surface defects is a crucial factor to realizing stable perovskite films and devices. We scrutinized the phase stability of the reference and DPA-TFA-incorporated perovskite films under exposure of ambient air with a 50% $\pm$ 10% relative humidity (RH). Figure S32A shows photographs of the perovskite films stored in the controlled environment. Clearly, DPA-TFA perovskite film maintained the initial α-$FAPbI_3$ (black) phase for 50 days, whereas the reference film gradually changed its color to yellow over time as a result of α-to-δ phase transition due to degradation. Quantitatively, we monitored the changes in δ-$FAPbI_3$ (010) to α-$FAPbI_3$ (100) XRD peak intensity ratios. For the reference film, a gradual increase of δ-$FAPbI_3$ (010) peak at the expense of α-$FAPbI_3$ (100) peak was observed, resulting in the α/δ intensity ratio of 31.8% after 50 days under exposure to ambient conditions (Figure S32B). In a stark contrast, no appreciable emergence of δ-$FAPbI_3$ (010) peak was observed in the DPA-TFA-incorporated film. These results clearly suggest that the incorporation of DPA-TFA enhances the phase stability of perovskite even under ambient humidity conditions, synergistically achieved by the comprehensive surface defect passivation of TFA^- through substantial non-covalent interaction and lattice protection against external stressors by bulky DPA^+.[33,41]

Inspired by the outstanding ambient phase stability of the DPA-TFA-incorporated perovskite film, we further explored the stability of the PSCs under humid air environments, which are known to accelerate the phase transition and thereby devastate the longevity of the devices.[63,64] DPA-TFA PSCs maintained over 92% of their maximum PCE (24.96%) for 10,000 h without encapsulation under dark conditions (ISOS-D-1) and in a controlled environment with <10% RH (Figure S33). However, for the reference device, only 77% of the maximum PCE (24.12%) was retained after 10,000 h.

Additionally, notable changes were observed upon 1,000 h of storage under various high-humidity conditions (i.e., 30%–80% RH; Figure 4F). Strikingly, the DPA-TFA-incorporated device maintained 98% of the initial PCE (24.42%) after 350 h under ~30% RH, which was subsequently dropped to 82% of the initial PCE after an additional 650 h under ~80% RH. By contrast, the reference device rapidly degraded and lost 16% of initial PCE (24.03%) after the first stage evaluation (under ~30% RH), which subsequently reached to 35% of the initial PCE after finishing the second stage of the stability test (under ~80% RH). Unequivocally, these observations indicate that such outstanding and unprecedent device stability is synergistically achieved by distinctive binding actions of DPA-TFA toward the perovskite surface.

DISCUSSION

Maximizing non-covalent interactions as design principles for perovskite passivating agents

Non-covalent interactions are well-known types of bonding to play an important role in the field of supramolecular chemistry, a field of study that concerns "chemistry beyond the molecule," i.e., systems comprising of multiple molecules and their collective structural/functional behavior.[65] In supramolecular chemistry, interactions between molecules as well as molecules and their matrix scaffold are of principal concern, a problem that closely resembles that in perovskite passivation, namely, the interaction between passivating (molecular) species and the perovskite scaffold.

Since supramolecular chemistry is already a mature field with many of the governing non-covalent interactions well-known to chemists, exploiting these interactions could open a new pathway for efficient passivation of perovskite surfaces. For instance, our current study shows that hydrogen bonding and dispersion (van der Waals) interactions, two bonding interactions that play key roles in important supramolecular phenomena such as DNA folding, drug binding, and molecular docking,[65–68] are also crucial for pseudohalide passivation; our previous work has also demonstrated the significance of hydrophobic interactions between moisture and aromatic DPA^+ cation for providing film stability against humid environments, a finding that directly translates to our present devices.[33] However, the key finding of our current study suggests that dispersion interaction plays a major role in determining the binding energy, which may serve as a design principle for discovering novel passivating agents. In addition, considering the plethora of other known supramolecular non-covalent interactions such as electrostatic, halogen bonding, π-π, and cation/anion-π interactions,[69,70] our work thus presents a new challenge for computational and synthetic chemists to predict and design a new family of strongly binding passivating agents exploiting these interactions, as well as materials scientists to build a "supramolecular assembly" of these molecules for efficient surface passivation of perovskite devices.

Conclusions

In summary, we present supramolecular non-covalent interactions as a design principle for efficient passivation of perovskite lattices. By using pseudohalides as a proof of concept, previously neglected non-covalent interactions such as hydrogen bonding and dispersion interactions are shown to be crucial in determining the binding ability of passivating species. Computational screening of pseudohalides predict TFA^- to be the strongest passivating agent for V_I at the perovskite surface and grain boundary, owing to the largest effective volume and ability to form non-covalent bonding through fluorine. On the cation side, we exploit the additional dispersion and hydrophobic interactions in DPA^+, which confer moisture stability as well as enhanced charge transport. Experimentally, our synergistic DPA-TFA passivation

indeed realizes comprehensive surface passivation and also manifests a homogenized α-$FAPbI_3$ lattice preferentially grown toward vertical direction, thus constructing a supramolecular-passivated perovskite matrix. Our discovery of DPA-TFA as a passivating agent in PSCs allows several remarkable performance metrics such as a PCE of 25.63%, a V_{OC} of 1.191 V, and stability over 1,000 h without encapsulation under humid environments, which translates to PSC modules with outstanding PCEs of 22.47% (QSS-certified at 20.50%) at 25 cm^2 and 20.73% at 64 cm^2. Considering the well-understood and essential nature of non-covalent interactions in supramolecular chemistry, our discovery unlocks a design principle for tuning the surface binding of functional passivating agents for perovskite-based devices such as solar cells, light emitting diodes, photodetectors, and transistors.

EXPERIMENTAL PROCEDURES

Resource availability

Lead contact

Further information and requests for resources should be directed to and will be fulfilled by the lead contact, Hyosung Choi (hschoi202@hanyang.ac.kr).

Materials availability

This study did not generate new unique reagents.

Data and code availability

This study did not generate or analyze datasets or code.

Materials

Fluorine-doped tin oxide on glass (FTO glass, 7 Ω sq^{-1}) substrate (Asahi), 2,2′,7,7′-tetrakis[N,N-di(4-methoxyphenyl)amino]-9,9′-spirobifluorene (Spiro-OMeTAD) was purchased from Lumtec. 3,3-Diphenylpropylamine (97%), hydroiodic acid (HI, 57 wt % in H_2O), trifluoroacetic acid (CF_3CO_2H, 99%), 2-methoxyethanol (2-ME, anhydrous 99.8%), 2-propanol (IPA, anhydrous, 99.5%), titanium diisopropoxide bis(acetylacetonate) (75 wt % in IPA), chlorobenzene (CB) (anhydrous, 99.8%), N,N-dimethylformamide (DMF, anhydrous 99.8%), dimethyl sulfoxide (DMSO, >99.5%), acetonitrile (ACN, anhydrous 99.8%), tetrahydrofuran (THF 99.9%), 4-tert-butylpyridine (tBP), lithium carbonate (Li_2CO_3), ethylenediaminetetraacetic acid (EDTA) solution, bis(trifluoromethane)sulfonimide lithium salt (Li-TFSi, 99.95% trace metals basis), tris(2-(1H-pyrazol-1-yl)-4-tertbutylpyridine) cobalt(III) (FK209), were purchased from Sigma Aldrich. Methylammonium chloride (MACl, 98%) was purchased from Acros Organics. Octylammonium iodide (OAI), FAI were purchased from GreatCell Solar. Acetic acid (99.5%), ethanol (absolute, 99.9%), and diethyl ether (extra pure grade) were purchased from Duksan. Aqueous solution of poly(3,4-ethylenedioxythiophene) polystyrene sulfonate (PEDOT:PSS, Clevios AI 4083) was purchased from Heraeus. Lead(II) iodide (PbI_2, 99.9985%) was purchased from Tokyo Chemical Industry (TCI). Tin(IV) oxide (SnO_2, 15 wt % in H_2O colloidal dispersion) was purchased from Alfa Aesar.

Synthesis of pseudohalide-based salts with DPA^+

DPA-TFA was prepared by slowly adding CF_3CO_2H (20 mmol) to a solution of 3,3-diphenylpropylamine (2.11 g, 10.0 mmol) in THF (10 mL) with ice-bath cooling and stirring. The resulting solution was stirred for 1 h at room temperature and then concentrated using a rotary evaporator. The remaining solid was washed three times with ethyl ether. Drying the product in a vacuum oven at 100°C yielded an off-white solid (3.21 g, 98.7% yield). Similarly, 3,3-DPA-Ac was prepared using the same experimental method as DPA-TFA, but acetic acid (1.20 g, 20 mmol) was used

instead. The product obtained was an off-white solid (2.55 g, 94.0% yield). 3,3-DPA iodide (DPA-I) was prepared using our previously reported method.[33]

Preparation of $FAPbI_3$ perovskite

$FAPbI_3$ black powder was synthesized, and 1.72 g FAI and 4.61 g PbI_2 (1:1 molar ratio) were dissolved in 2-ME (0.6 M) first and then filtered using a polyvinylidene fluoride (PVDF) filter with 0.45 μm pore size. The filtered solution was placed in a flask incubated in an oil bath at 120°C for 1 h under slow stirring. The resulting black powder was filtered using a glass filter and dried at 100°C for 24 h.

Computational calculation

All *ab initio* calculations were performed with the Vienna Ab initio Simulation Package (VASP 5.4.4).[71–74] The projector augmented wave (PAW) method[73–76] was employed, and exchange-correlation interactions were treated through Perdew-Burke-Ernzerohf (PBE)[77] functional under the generalized gradient approximation (GGA). We used a Γ-centered 3 × 3 × 3 *k*-point mesh in each primitive lattice vector of the reciprocal space for bulk structure geometric optimization and changed the mesh as a Monkhorst-Pack 2 × 2 × 1 *k*-point mesh for surface structure geometric optimization, respectively, for Brillouin zone sampling.[78] In addition, to adjust non-covalent interactions in our system, we used DFT-D3 dispersion correction methods to reflect the vdW (van der Waals) correlation in the $FAPbI_3$ system with considering the spin-polarization effect.[77,79] A plane-wave cutoff energy of 500 eV was used lattice constants and internal atomic positions were fully optimized until the residual forces were less than 0.04 eV/Å. The detailed information on structure modeling and estimated properties related to $FAPbI_3$ was explained in Notes S1–S3.

Fabrication of PSCs

FTO glass (Asahi) was cleaned using the RCA-2 (H_2O_2:HCl:H_2O = 1:1:5) procedure for 15 min in an ultrasonic bath and then washed sequentially with acetone and IPA for 10 min each. For fabricating the compact TiO_2 (c-TiO_2) layer, which was deposited by spray coating, 40 mL of a titanium diisopropoxide bis(acetylacetonate)/ethanol (1:10) solution was sprayed using a spray gun at 450°C for 20 min with oxygen at a speed of 4 L/min. After completing the c-TiO_2 layer, the substrates were stored at 450°C for 1 h. The thickness of c-TiO_2 is about 20 nm. Long time and low-concentration spray-coating process is recommended for a well-defined c-TiO_2 layer. In the case where the SnO_2 layer was deposited by spin-coating, SnO_2 was diluted 20 times with distilled water and then mixed with EDTA solution (1 mg/mL) under stirring at 80°C for 2 h. The resulting solution was spin-coated onto the c-TiO_2 layer at 4,000 rpm for 30 s. The substrates were heated at 100°C for 30 min under a vacuum condition. Before spin-coating the perovskite layer, the substrate was treated with Li_2CO_3 (0.5 mg/mL) and annealed at 100°C for another 30 min under a vacuum condition. The perovskite precursor solution was prepared by dissolving 1,446 mg $FAPbI_3$ black powder and 46.6 mg MACl with 1 mL DMF/DMSO (4:1). For DPA-X* incorporation, appropriate amounts of the DPA-X* salts with targeted concentrations (mol % with respect to $FAPbI_3$) are added to the precursor solution. The perovskite solution was filtered with a PVDF filter (0.2 μm), and then 70 μL of the filtered perovskite solution was spread onto different electron transport layers at 8,000 rpm for 50 s. Before coating, the substrates were treated with plasma for 5 min. During the spin-coating, 1 mL diethyl ether was dropped on the perovskite film at 10 s using a homemade pipette. The resulting film was annealed at 150°C for 15 min and 100°C for 30 min on a hotplate. After the substrates cooling down, OAI in IPA solution (15 mM) was spin-coated on the perovskite layer at 3,000 rpm for 30 s. For the hole transport layer was deposited by spin-coating,

the Spiro-OMeTAD solution was spin-coated on the perovskite layer at 4,000 rpm for 30 s. Spiro-OMeTAD (90 mg/mL in CB) was doped with 39 μL tBP, 23 μL Li-TFSI (520 mg/mL in ACN), and 5 μL FK209 (180 mg/mL in ACN). All these processes were carried out in ambient environment at strictly controlled 25% RH and at 25°C. Finally, the gold electrode was deposited onto the Spiro-OMeTAD layer using a thermal evaporation system. 80 nm thick gold was deposited at 2 Å/s under a pressure of 10^{-6} Torr.

Characterization of the perovskite films

SEM images of perovskite films were taken using a FE-SEM, S-4800 (Hitachi). The 2D-GIWAXS measurements were carried out at the 9A beamline (U-SAXS) at the Pohang Accelerator Laboratory in Pohang, Republic of Korea. The beam energy used was 11.07 KeV, and the incident angles were set at 0.12°. The samples were spin-coated onto an FTO/c-TiO_2/SnO_2 substrate. UV-vis absorption spectra were obtained using a UV-vis spectrometer, UV-2600 (Shimadzu). Steady-state PL and TRPL measurements of the perovskite films were performed using a PicoQuant FluoTime 300 system (PicoQuant) equipped with a PLP-10 laser diode head and an M10306 driver. A pulsed laser diode operating at a wavelength of 375 nm, with a peak power of 600 mW, a pulse width of 50 ps, and a repetition rate of 80 MHz, was utilized. The laser pulse diameter was set at 8 mm. TRPL measurements were conducted under an excitation fluence of 4.775×10^4 mJ/cm^2. NMR measurements were performed at 9.4 T (KBSI Western Seoul Center) using a 4 mm Bruker HXY probe. Perovskite films with DPA-TFA treatment were prepared by spin-coating the precursor solution on glass substrates and which were subsequently scraped to obtain powder of thin films. The collected powder was packed in zirconia rotors and spun at 12.5 kHz magic angle spinning (MAS) using vespel caps. ^{13}C spectra were acquired using ^{1}H-^{13}C and ^{19}F-^{13}C Hartmann-Hahn CP sequence with 100 kHz SPINAL64 ^{1}H or ^{19}F decoupling. ^{13}C and ^{19}F shifts were referenced to tetramethylsilane and CF_3CO_2H (−76.55 ppm), respectively. Recycle delays of 10 s were used for all spectra. XPS measurements were carried out with a K-alpha photoelectron spectrometer (Thermo Fisher Scientific) at the Hanyang LNC 3.0 Analytical Equipment Center (Seoul). The X-ray source utilized for the measurements was Al Kα (1,486.7 eV). XRD patterns of the perovskite films were obtained using a Rigaku SmartLab diffractometer. Hyperspectral CL microscopy data were collected by using an environmental SEM instrument (FEI, Quattro) with a Delmic Sparc CL collection module. A parabolic mirror is utilized to collect the CL signals upon e-beam excitation. An e-beam with an acceleration voltage of 5 kV (beam current of 28 pA) with a short acquisition time of 150 ms was used for CL measurements. A fixed 40×40 nm^2 pixel size was used. All measurements were conducted in a low vacuum environment of 0.02 Torr with H_2O vapor, which effectively alleviated sample charging while minimizing electron-beam-induced damage.

Fabrication of perovskite solar mini modules

For the perovskite mini modules of 25 and 64 cm^2, FTO etching was performed, with three different process recipes (denoted P1, P2, and P3). In the P1 process, FTO substrates of sizes 6.5 cm × 6.5 cm and 9.5 cm × 9.5 cm were patterned using a picosecond laser (Advance Optowave, AMT 532) with a power of 1.7 W, employing a scribing width of 20 μm and connecting 10 and 16 strips in series. The fabrication of the electron transport layer (ETL) involved spray-coating c-TiO_2 and spin-coating SnO_2, following the same procedure as for the small-size cells. For the deposition of the perovskite layer, 1,329.3 mg of $FAPbI_3$ and 49.6 mg of MACl were dissolved in 1 mL of DMF/DMSO (4:1). Subsequently, 150 μL of the filtered solution was applied to the substrate and spin-coated at 5,000 rpm for 50 s. The coated perovskite layer

was then baked at 150°C for 15 min and 100°C for 30 min. The hole transport layer was deposited using the same method as described above. In the P2 process, laser scribing with a power of 0.8 W and a width of 56 μm was performed, with a distance of about 5 μm between P1 and P2. Finally, the Au counter electrode was deposited with a thickness of 80 nm. In the P3 process, the Au layer was scribed with a width of 25 μm, and the distance between P2 and P3 was approximately 40 μm.

Characterization of the perovskite devices

The PSCs were measured using a solar simulator (Newport-Oriel 94083A, Class AAA) in conjunction with a Keithley source meter 2400 while maintaining ambient conditions (25% RH at 25°C). The light intensity was calibrated to 100 mW/cm^2 using an NREL-certified Si-reference cell. To restrict the active cell area to 0.0803 cm^2, the PSCs of a specific size were masked using a shadow metal mask. For mini modules with sizes of 25 and 64 cm^2, voltage ranges were set at 12.5–0 V and 20–0 V, respectively. In the case of the PSC mini module, it was precisely cut to the desired size using a laser, and the edges were covered with black tape. The stabilized power output was measured at the MPP using a xenon lamp as the light source. EQE measurements were carried out for the PSCs using a QEX7 system (PV Measurement) The PSCs were measured using a solar simulator (Newport-Oriel 94083A, Class AAA) in combination with a Keithley source meter 2400. MPP tracking of the PSCs was conducted under continuous illumination, while the temperature was maintained at 20°C during the measurements. Reverse-scanned *J-V* curves were recorded at intervals of 1 s. In order to evaluate the operational stability of the encapsulated devices, the cells were measured under the MPP tracking condition in an ambient environment with 25% RH at 25°C (Solixion A-45-TE, SOLARONIX). The TPV measurements were conducted using a home-built setup consisting of a pulsed Nd:YAG laser (VIBRANT 355 LD, OPOTEK) with a repetition rate of 10 Hz and a pulse width of 5 ns, an oscilloscope (Agilent DSO3202A), and additional light output from a xenon lamp.[80,81] The V_{OC} generated by the continuous light was monitored using a Keithley 2400 sourcemeter. A small perturbation using a laser pulse with a wavelength of 532 nm was applied to the samples, and the fluence was modulated using a series of neutral-density filters. A 1 MΩ input terminal resistor was connected to the oscilloscope for TPV measurements. The SCLC measurements of the hole-only devices (FTO/PEDOT:PSS/perovskite/Spiro-OMeTAD/Au) were conducted with a Keithley 2400 sourcemeter. Based on the *J-V* curves, V_{TFL} was calculated as follows:

$$V_{TFL} = \frac{qN_tL^2}{2\varepsilon\varepsilon_0} \quad \text{(Equation 1)}$$

where V_{TFL} is the trap-filled limit voltage, q the elementary charge, L the thickness of the perovskite film, ε the relative dielectric constant (46.9), and ε_0 the vacuum permittivity.[82]

SUPPLEMENTAL INFORMATION

Supplemental information can be found online at https://doi.org/10.1016/j.joule.2024.05.019.

ACKNOWLEDGMENTS

This research was supported by the Nano·Material Technology Development Program through the National Research Foundation of Korea (NRF), funded by the Ministry of Science and ICT (NRF-2021M3H4A1A02049634 and NRF-2022R1A2C1002764). This research was supported by the BrainLink program funded by the Ministry of Science of ICT through the National Research Foundation of Korea

(NRF-2022H1D3A3A01077343). This research was supported by the Basic Science Research Program through the National Research Foundation of Korea (NRF), funded by the Ministry of Education (RS-2023-00276169). This work was supported by the Basic Science Research Program of the National Research Foundation of Korea (NRF-2021R1A2B5B01002879). Y.J. acknowledges support from the Technology Development Program to Solve Climate Changes of the National Research Foundation (NRF), funded by the Ministry of Science, ICT & Future Planning (2020M1A2A2080746) and the Development Program of the Korea Institute of Energy Research (KIER) (C4-2414 and C4-2460). J.Yang and M.A. acknowledge support from the National Science Foundation (NSF), award no. 2043205, and the Alfred P. Sloan Foundation (award no. FG-2022-18275). The CL microscopy was supported by the Center for Nanophase Materials Sciences (CNMS) user facility, project CNMS2022-A-01171, which is a US Department of Energy, Office of Science User Facility at Oak Ridge National Laboratory. Solid-state NMR measurements were conducted at the KBSI Western Seoul Center 9.4 T magnet. We thank Dr Young Joo Lee and Dokyung Kim for helping with NMR measurements.

AUTHOR CONTRIBUTIONS

H.S. and H.C. initially conceptualized the work. H.-B.K., H.S., and J.Y.W. prepared the samples and conducted device fabrications and general characterizations. H.-B.K. and D.S.K. fabricated PSC mini modules. M.L. synthesized the DPA-X* salt. S.C.C. and S.U.L. contributed to computational calculations. W.H.J. and B.R.L. conducted steady-state PL and TRPL measurements. J.L. analyzed NMR spectroscopic data. J. Yeop and J.Y.K. carried out GIWAXS measurements. J. Yang, B.J.L., and M.A. conducted hyperspectral CL microscopy. M.K. and S.J.C. collected the light-intensity-dependent *J-V* data. H.S. wrote the draft with help from H.-B.K., J. Yang, W.H.J., and H.I.J. H.S., J. Yang, J.L., and H.C. revised and prepared the manuscript. M.L., S.U.L., Y.J., and H.C. supervised the project. All authors contributed to discussions and the preparation of the manuscript.

DECLARATION OF INTERESTS

The authors declare no competing interests.

Received: February 19, 2024
Revised: March 19, 2024
Accepted: May 30, 2024
Published: June 19, 2024

REFERENCES

1. Kojima, A., Teshima, K., Shirai, Y., and Miyasaka, T. (2009). Organometal Halide Perovskites as Visible-Light Sensitizers for Photovoltaic Cells. J. Am. Chem. Soc. *131*, 6050–6051. https://doi.org/10.1021/ja809598r.

2. Kim, J.Y., Lee, J.-W., Jung, H.S., Shin, H., and Park, N.-G. (2020). High-Efficiency Perovskite Solar Cells. Chem. Rev. *120*, 7867–7918. https://doi.org/10.1021/acs.chemrev.0c00107.

3. Huang, Y., Lei, X., He, T., Jiang, Y., and Yuan, M. (2022). Recent Progress on Formamidinium-Dominated Perovskite Photovoltaics. Adv. Energy Mater. *12*, 2100690. https://doi.org/10.1002/aenm.202100690.

4. Mannino, G., Deretzis, I., Smecca, E., La Magna, A., Alberti, A., Ceratti, D., and Cahen, D. (2020). Temperature-Dependent Optical Band Gap in CsPbBr3, MAPbBr3, and FAPbBr3 Single Crystals. J. Phys. Chem. Lett. *11*, 2490–2496. https://doi.org/10.1021/acs.jpclett.0c00295.

5. Smecca, E., Numata, Y., Deretzis, I., Pellegrino, G., Boninelli, S., Miyasaka, T., La Magna, A., and Alberti, A. (2016). Stability of solution-processed $MAPbI_3$ and $FAPbI_3$ layers. Phys. Chem. Chem. Phys. *18*, 13413–13422. https://doi.org/10.1039/C6CP00721J.

6. Park, J., Kim, J., Yun, H.-S., Paik, M.J., Noh, E., Mun, H.J., Kim, M.G., Shin, T.J., and Seok, S.I. (2023). Controlled growth of perovskite layers with volatile alkylammonium chlorides. Nature *616*, 724–730. https://doi.org/10.1038/s41586-023-05825-y.

7. Rühle, S. (2016). Tabulated values of the Shockley–Queisser limit for single junction solar cells. Sol. Energy *130*, 139–147. https://doi.org/10.1016/j.solener.2016.02.015.

8. Lin, H., Yang, M., Ru, X., Wang, G., Yin, S., Peng, F., Hong, C., Qu, M., Lu, J., Fang, L., et al. (2023). Silicon heterojunction solar cells with up to 26.81% efficiency achieved by electrically optimized nanocrystalline-silicon hole contact layers. Nat. Energy *8*, 789–799. https://doi.org/10.1038/s41560-023-01255-2.

9. Nayak, P.K., Mahesh, S., Snaith, H.J., and Cahen, D. (2019). Photovoltaic solar cell technologies: analysing the state of the art. Nat. Rev. Mater. *4*, 269–285. https://doi.org/10.1038/s41578-019-0097-0.

10. Guo, Z., Jena, A.K., Kim, G.M., and Miyasaka, T. (2022). The high open-circuit voltage of perovskite solar cells: a review. Energy Environ.

Sci. *15*, 3171–3222. https://doi.org/10.1039/D2EE00663D.

11. Luo, D., Su, R., Zhang, W., Gong, Q., and Zhu, R. (2020). Minimizing non-radiative recombination losses in perovskite solar cells. Nat. Rev. Mater. *5*, 44–60. https://doi.org/10.1038/s41578-019-0151-y.

12. Fang, Z., Sun, J., Liu, S., and Ding, L. (2023). Defects in perovskite crystals. J. Semicond. *44*, 080201. https://doi.org/10.1088/1674-4926/44/8/080201.

13. Yang, J., Sharma, A., Yoon, J.W., Paritmongkol, W., Lee, S., Ahn, H., Lee, W., Song, H., Jeong, W.H., Lee, B.R., et al. (2023). Structurally Driven Ultrafast Charge Funneling in Organic Bulk Heterojunction Hole Transport Layer for Efficient Colloidal Quantum Dot Photovoltaics. Adv. Energy Mater. *13*, 2203749. https://doi.org/10.1002/aenm.202203749.

14. Yang, J., LaFollette, D.K., Lawrie, B.J., Ievlev, A.V., Liu, Y., Kelley, K.P., Kalinin, S.V., Correa-Baena, J.-P., and Ahmadi, M. (2023). Understanding the Role of Cesium on Chemical Complexity in Methylammonium-Free Metal Halide Perovskites. Adv. Energy Mater. *13*, 2202880. https://doi.org/10.1002/aenm.202202880.

15. Yang, X., Ni, Y., Zhang, Y., Wang, Y., Yang, W., Luo, D., Tu, Y., Gong, Q., Yu, H., and Zhu, R. (2021). Multiple-Defect Management for Efficient Perovskite Photovoltaics. ACS Energy Lett. *6*, 2404–2412. https://doi.org/10.1021/acsenergylett.1c01039.

16. Wu, W.-Q., Rudd, P.N., Ni, Z., Van Brackle, C.H., Wei, H., Wang, Q., Ecker, B.R., Gao, Y., and Huang, J. (2020). Reducing Surface Halide Deficiency for Efficient and Stable Iodide-Based Perovskite Solar Cells. J. Am. Chem. Soc. *142*, 3989–3996. https://doi.org/10.1021/jacs.9b13418.

17. Jin, H., Debroye, E., Keshavarz, M., Scheblykin, I.G., Roeffaers, M.B.J., Hofkens, J., and Steele, J.A. (2020). It's a trap! On the nature of localised states and charge trapping in lead halide perovskites. Mater. Horiz. *7*, 397–410. https://doi.org/10.1039/C9MH00500E.

18. Mohd Yusoff, A.R.b., Vasilopoulou, M., Georgiadou, D.G., Palilis, L.C., Abate, A., and Nazeeruddin, M.K. (2021). Passivation and process engineering approaches of halide perovskite films for high efficiency and stability perovskite solar cells. Energy Environ. Sci. *14*, 2906–2953. https://doi.org/10.1039/D1EE00062D.

19. Li, N., Tao, S., Chen, Y., Niu, X., Onwudinanti, C.K., Hu, C., Qiu, Z., Xu, Z., Zheng, G., Wang, L., et al. (2019). Cation and anion immobilization through chemical bonding enhancement with fluorides for stable halide perovskite solar cells. Nat. Energy *4*, 408–415. https://doi.org/10.1038/s41560-019-0382-6.

20. Lin, P.-Y., Loganathan, A., Raifuku, I., Li, M.-H., Chiu, Y.-Y., Chang, S.-T., Fakharuddin, A., Lin, C.-F., Guo, T.-F., Schmidt-Mende, L., et al. (2021). Pseudo-Halide Perovskite Solar Cells. Adv. Energy Mater. *11*, 2100818. https://doi.org/10.1002/aenm.202100818.

21. Tan, S., Huang, T., Yavuz, I., Wang, R., Yoon, T.W., Xu, M., Xing, Q., Park, K., Lee, D.-K., Chen, C.-H., et al. (2022). Stability-limiting heterointerfaces of perovskite photovoltaics. Nature *605*, 268–273. https://doi.org/10.1038/s41586-022-04604-5.

22. Song, H., Yang, J., Lim, S.G., Lee, J., Jeong, W.H., Choi, H., Lee, J.H., Kim, H.Y., Lee, B.R., and Choi, H. (2023). On the surface passivating principle of functional thiol towards efficient and stable perovskite nanocrystal solar cells. Chem. Eng. J. *454*, 140224. https://doi.org/10.1016/j.cej.2022.140224.

23. Tao, J., Liu, X., Shen, J., Han, S., Guan, L., Fu, G., Kuang, D.-B., and Yang, S. (2022). F-Type Pseudo-Halide Anions for High-Efficiency and Stable Wide-Band-Gap Inverted Perovskite Solar Cells with Fill Factor Exceeding 84%. ACS Nano *16*, 10798–10810. https://doi.org/10.1021/acsnano.2c02876.

24. Li, S., Xia, J., Wen, Z., Gu, H., Guo, J., Liang, C., Pan, H., Wang, X., and Chen, S. (2023). The Formation Mechanism of (001) Facet Dominated α-FAPbI3 Film by Pseudohalide Ions for High-Performance Perovskite Solar Cells. Adv. Sci. (Weinh) *10*, e2300056. https://doi.org/10.1002/advs.202300056.

25. Bu, T., Li, J., Li, H., Tian, C., Su, J., Tong, G., Ono, L.K., Wang, C., Lin, Z., Chai, N., et al. (2021). Lead halide–templated crystallization of methylamine-free perovskite for efficient photovoltaic modules. Science *372*, 1327–1332. https://doi.org/10.1126/science.abh1035.

26. Kim, D., Jung, H.J., Park, I.J., Larson, B.W., Dunfield, S.P., Xiao, C., Kim, J., Tong, J., Boonmongkolras, P., Ji, S.G., et al. (2020). Efficient, stable silicon tandem cells enabled by anion-engineered wide-bandgap perovskites. Science *368*, 155–160. https://doi.org/10.1126/science.aba3433.

27. Yang, J., Cho, S.C., Lee, S., Yoon, J.W., Jeong, W.H., Song, H., Oh, J.T., Lim, S.G., Bae, S.Y., Lee, B.R., et al. (2022). Guanidinium-Pseudohalide Perovskite Interfaces Enable Surface Reconstruction of Colloidal Quantum Dots for Efficient and Stable Photovoltaics. ACS Nano *16*, 1649–1660. https://doi.org/10.1021/acsnano.1c10636.

28. Jeong, J., Kim, M., Seo, J., Lu, H., Ahlawat, P., Mishra, A., Yang, Y., Hope, M.A., Eickemeyer, F.T., Kim, M., et al. (2021). Pseudo-halide anion engineering for α-$FAPbI_3$ perovskite solar cells. Nature *592*, 381–385. https://doi.org/10.1038/s41586-021-03406-5.

29. Pandech, N., Kongnok, T., Palakawong, N., Limpijumnong, S., Lambrecht, W.R.L., and Jungthawan, S. (2020). Effects of the van der Waals Interactions on Structural and Electronic Properties of $CH_3NH_3(Pb,Sn)(I,Br,Cl)_3$ Halide Perovskites. ACS Omega *5*, 25723–25732. https://doi.org/10.1021/acsomega.0c03016.

30. Zheng, Y., Fang, Z., Shang, M., Sun, Q., Hou, X., and Yang, W. (2023). Are formation and adsorption energies enough to evaluate the stability of surface-passivated tin-based halide perovskites? Mater. Horiz. *10*, 2691–2697. https://doi.org/10.1039/D3MH00221G.

31. Dong, Z., Luo, Q., and Liu, J. (2012). Artificial enzymes based on supramolecular scaffolds. Chem. Soc. Rev. *41*, 7890–7908. https://doi.org/10.1039/C2CS35207A.

32. Pieters, B.J.G.E., van Eldijk, M.B., Nolte, R.J.M., and Mecinović, J. (2016). Natural supramolecular protein assemblies. Chem. Soc. Rev. *45*, 24–39. https://doi.org/10.1039/C5CS00157A.

33. Song, H., Yang, J., Jeong, W.H., Lee, J., Lee, T.H., Yoon, J.W., Lee, H., Ramadan, A.J., Oliver, R.D.J., Cho, S.C., et al. (2023). A Universal Perovskite Nanocrystal Ink for High-Performance Optoelectronic Devices. Adv. Mater. *35*, e2209486. https://doi.org/10.1002/adma.202209486.

34. Li, P., Maier, J.M., Vik, E.C., Yehl, C.J., Dial, B.E., Rickher, A.E., Smith, M.D., Pellechia, P.J., and Shimizu, K.D. (2017). Stabilizing Fluorine–π Interactions. Angew. Chem. Int. Ed. Engl. *56*, 7209–7212. https://doi.org/10.1002/anie.201702950.

35. Chopra, D., and Row, T.N.G. (2011). Role of organic fluorine in crystal engineering. CrystEngComm *13*, 2175–2186. https://doi.org/10.1039/C0CE00538J.

36. Chopra, D. (2012). Is Organic Fluorine Really "Not" Polarizable? Cryst. Growth Des. *12*, 541–546. https://doi.org/10.1021/cg201498u.

37. Li, M., Sun, R., Chang, J., Dong, J., Tian, Q., Wang, H., Li, Z., Yang, P., Shi, H., Yang, C., et al. (2023). Orientated crystallization of FA-based perovskite via hydrogen-bonded polymer network for efficient and stable solar cells. Nat. Commun. *14*, 573. https://doi.org/10.1038/s41467-023-36224-6.

38. Liang, J., Hu, X., Wang, C., Liang, C., Chen, C., Xiao, M., Li, J., Tao, C., Xing, G., Yu, R., et al. (2022). Origins and influences of metallic lead in perovskite solar cells. Joule *6*, 816–833. https://doi.org/10.1016/j.joule.2022.03.005.

39. McGettrick, J.D., Hooper, K., Pockett, A., Baker, J., Troughton, J., Carnie, M., and Watson, T. (2019). Sources of Pb(0) artefacts during XPS analysis of lead halide perovskites. Mater. Lett. *251*, 98–101. https://doi.org/10.1016/j.matlet.2019.04.081.

40. Hofstetter, Y.J., García-Benito, I., Paulus, F., Orlandi, S., Grancini, G., and Vaynzof, Y. (2020). Vacuum-Induced Degradation of 2D Perovskites. Front. Chem. *8*, 66. https://doi.org/10.3389/fchem.2020.00066.

41. Tan, S., Yavuz, I., Weber, M.H., Huang, T., Chen, C.-H., Wang, R., Wang, H.-C., Ko, J.H., Nuryyeva, S., Xue, J., et al. (2020). Shallow Iodine Defects Accelerate the Degradation of α-Phase Formamidinium Perovskite. Joule *4*, 2426–2442. https://doi.org/10.1016/j.joule.2020.08.016.

42. Lee, J.-W., Dai, Z., Han, T.-H., Choi, C., Chang, S.-Y., Lee, S.-J., De Marco, N., Zhao, H., Sun, P., Huang, Y., et al. (2018). 2D perovskite stabilized phase-pure formamidinium perovskite solar cells. Nat. Commun. *9*, 3021. https://doi.org/10.1038/s41467-018-05454-4.

43. Seo, H.-K., Kim, H., Lee, J., Park, M.-H., Jeong, S.-H., Kim, Y.-H., Kwon, S.-J., Han, T.-H., Yoo, S., and Lee, T.-W. (2017). Efficient Flexible Organic/Inorganic Hybrid Perovskite Light-Emitting Diodes Based on Graphene Anode.

Adv. Mater. *29*, 1605587. https://doi.org/10.1002/adma.201605587.

44. Jeong, W.H., Yu, Z., Gregori, L., Yang, J., Ha, S.R., Jang, J.W., Song, H., Park, J.H., Jung, E.D., Song, M.H., et al. (2021). In situ cadmium surface passivation of perovskite nanocrystals for blue LEDs. J. Mater. Chem. A *9*, 26750–26757. https://doi.org/10.1039/D1TA08756H.

45. Zhao, X., Ball, M.L., Kakekhani, A., Liu, T., Rappe, A.M., and Loo, Y.-L. (2022). A charge transfer framework that describes supramolecular interactions governing structure and properties of 2D perovskites. Nat. Commun. *13*, 3970. https://doi.org/10.1038/s41467-022-31567-y.

46. Yang, J., Hidalgo, J., Kalinin, S.V., Correa-Baena, J.P., and Ahmadi, M. (2023). Accelerating Materials Discovery by High-Throughput GIWAXS Characterization of Quasi-2D Formamidinium Metal Halide Perovskites. Preprint at ChemRxiv. https://doi.org/10.26434/chemrxiv-2023-x7sfr-v2.

47. Hidalgo, J., Atourki, L., Li, R., Castro-Méndez, A.-F., Kim, S., Sherman, E.A., Bieber, A.S., Sher, M.-j., Nienhaus, L., Perini, C.A.R., et al. (2023). Bulky cation hinders undesired secondary phases in $FAPbI_3$ perovskite solar cells. Mater. Today *68*, 13–21. https://doi.org/10.1016/j.mattod.2023.06.010.

48. Hidalgo, J., Perini, C.A.R., Castro-Mendez, A.-F., Jones, D., Köbler, H., Lai, B., Li, R., Sun, S., Abate, A., and Correa-Baena, J.-P. (2020). Moisture-Induced Crystallographic Reorientations and Effects on Charge Carrier Extraction in Metal Halide Perovskite Solar Cells. ACS Energy Lett. *5*, 3526–3534. https://doi.org/10.1021/acsenergylett.0c01964.

49. Macpherson, S., Doherty, T.A.S., Winchester, A.J., Kosar, S., Johnstone, D.N., Chiang, Y.-H., Galkowski, K., Anaya, M., Frohna, K., Iqbal, A.N., et al. (2022). Local nanoscale phase impurities are degradation sites in halide perovskites. Nature *607*, 294–300. https://doi.org/10.1038/s41586-022-04872-1.

50. Du, T., Richheimer, F., Frohna, K., Gasparini, N., Mohan, L., Min, G., Xu, W., Macdonald, T.J., Yuan, H., Ratnasingham, S.R., et al. (2022). Overcoming Nanoscale Inhomogeneities in Thin-Film Perovskites via Exceptional Post-annealing Grain Growth for Enhanced Photodetection. Nano Lett. *22*, 979–988. https://doi.org/10.1021/acs.nanolett.1c03839.

51. Frohna, K., Anaya, M., Macpherson, S., Sung, J., Doherty, T.A.S., Chiang, Y.-H., Winchester, A.J., Orr, K.W.P., Parker, J.E., Quinn, P.D., et al. (2022). Nanoscale chemical heterogeneity dominates the optoelectronic response of alloyed perovskite solar cells. Nat. Nanotechnol. *17*, 190–196. https://doi.org/10.1038/s41565-021-01019-7.

52. Doherty, T.A.S., Nagane, S., Kubicki, D.J., Jung, Y.-K., Johnstone, D.N., Iqbal, A.N., Guo, D., Frohna, K., Danaie, M., Tennyson, E.M., et al. (2021). Stabilized tilted-octahedra halide perovskites inhibit local formation of performance-limiting phases. Science *374*, 1598–1605. https://doi.org/10.1126/science.abl4890.

53. Ma, F., Li, J., Li, W., Lin, N., Wang, L., and Qiao, J. (2017). Stable α/δ phase junction of formamidinium lead iodide perovskites for enhanced near-infrared emission. Chem. Sci. *8*, 800–805. https://doi.org/10.1039/C6SC03542F.

54. Ye, F., Zhang, S., Warby, J., Wu, J., Gutierrez-Partida, E., Lang, F., Shah, S., Saglamkaya, E., Sun, B., Zu, F., et al. (2022). Overcoming C_{60}-induced interfacial recombination in inverted perovskite solar cells by electron-transporting carborane. Nat. Commun. *13*, 7454. https://doi.org/10.1038/s41467-022-34203-x.

55. Li, T., Xu, J., Lin, R., Teale, S., Li, H., Liu, Z., Duan, C., Zhao, Q., Xiao, K., Wu, P., et al. (2023). Inorganic wide-bandgap perovskite subcells with dipole bridge for all-perovskite tandems. Nat. Energy *8*, 610–620. https://doi.org/10.1038/s41560-023-01250-7.

56. Liu, Y., Yang, J., Lawrie, B.J., Kelley, K.P., Ziatdinov, M., Kalinin, S.V., and Ahmadi, M. (2023). Disentangling Electronic Transport and Hysteresis at Individual Grain Boundaries in Hybrid Perovskites via Automated Scanning Probe Microscopy. ACS Nano *17*, 9647–9657. https://doi.org/10.1021/acsnano.3c03363.

57. Liu, Y., Yang, J., Vasudevan, R.K., Kelley, K.P., Ziatdinov, M., Kalinin, S.V., and Ahmadi, M. (2023). Exploring the Relationship of Microstructure and Conductivity in Metal Halide Perovskites via Active Learning-Driven Automated Scanning Probe Microscopy. J. Phys. Chem. Lett. *14*, 3352–3359. https://doi.org/10.1021/acs.jpclett.3c00223.

58. Hao, M., Duan, T., Ma, Z., Ju, M.-G., Bennett, J.A., Liu, T., Guo, P., and Zhou, Y. (2023). Flattening Grain-Boundary Grooves for Perovskite Solar Cells with High Optomechanical Reliability. Adv. Mater. *35*, e2211155. https://doi.org/10.1002/adma.202211155.

59. Yang, D., Zhou, X., Yang, R., Yang, Z., Yu, W., Wang, X., Li, C., Liu, S., and Chang, R.P.H. (2016). Surface optimization to eliminate hysteresis for record efficiency planar perovskite solar cells. Energy Environ. Sci. *9*, 3071–3078. https://doi.org/10.1039/C6EE02139E.

60. Son, D.-Y., Kim, S.-G., Seo, J.-Y., Lee, S.-H., Shin, H., Lee, D., and Park, N.-G. (2018). Universal Approach toward Hysteresis-Free Perovskite Solar Cell via Defect Engineering. J. Am. Chem. Soc. *140*, 1358–1364. https://doi.org/10.1021/jacs.7b10430.

61. Khenkin, M.V., Katz, E.A., Abate, A., Bardizza, G., Berry, J.J., Brabec, C., Brunetti, F., Bulović, V., Burlingame, Q., Di Carlo, A., et al. (2020). Consensus statement for stability assessment and reporting for perovskite photovoltaics based on ISOS procedures. Nat. Energy *5*, 35–49. https://doi.org/10.1038/s41560-019-0529-5.

62. Wolff, C.M., Caprioglio, P., Stolterfoht, M., and Neher, D. (2019). Nonradiative Recombination in Perovskite Solar Cells: The Role of Interfaces. Adv. Mater. *31*, e1902762. https://doi.org/10.1002/adma.201902762.

63. Wozny, S., Yang, M., Nardes, A.M., Mercado, C.C., Ferrere, S., Reese, M.O., Zhou, W., and Zhu, K. (2015). Controlled Humidity Study on the Formation of Higher Efficiency Formamidinium Lead Triiodide-Based Solar Cells. Chem. Mater. *27*, 4814–4820. https://doi.org/10.1021/acs.chemmater.5b01691.

64. Yun, J.S., Kim, J., Young, T., Patterson, R.J., Kim, D., Seidel, J., Lim, S., Green, M.A., Huang, S., and Ho-Baillie, A. (2018). Humidity-Induced Degradation via Grain Boundaries of HC(NH2)2PbI3 Planar Perovskite Solar Cells. Adv. Funct. Mater. *28*, 1705363. https://doi.org/10.1002/adfm.201705363.

65. Lehn, J.M. (1993). Supramolecular Chemistry. Science *260*, 1762–1763. https://doi.org/10.1126/science.8511582.

66. Phlip, D. (1996). Supramolecular chemistry: Concepts and perspectives. By J.-M. Lehn, VCH, Weinheim 1995, x, 271 pp., softcover, DM 58.00, ISBN 3-527-2931 1-6. Adv. Mater. *8*, 866–868. https://doi.org/10.1002/adma.19960081029.

67. Lehn, J.M. (1985). Supramolecular Chemistry: Receptors, Catalysts, and Carriers. Science *227*, 849–856. https://doi.org/10.1126/science.227.4689.849.

68. Menger, F.M. (2002). Supramolecular chemistry and self-assembly. Proc. Natl. Acad. Sci. USA *99*, 4818–4822. https://doi.org/10.1073/pnas.062524299.

69. Biedermann, F., and Schneider, H.-J. (2016). Experimental Binding Energies in Supramolecular Complexes. Chem. Rev. *116*, 5216–5300. https://doi.org/10.1021/acs.chemrev.5b00583.

70. Schneider, H.-J. (2009). Binding Mechanisms in Supramolecular Complexes. Angew. Chem. Int. Ed. Engl. *48*, 3924–3977. https://doi.org/10.1002/anie.200802947.

71. Kresse, G., and Hafner, J. (1993). Ab initio molecular dynamics for open-shell transition metals. Phys. Rev. B Condens. Matter *48*, 13115–13118. https://doi.org/10.1103/PhysRevB.48.13115.

72. Kresse, G., and Hafner, J. (1994). Ab initio molecular-dynamics simulation of the liquid-metal—amorphous-semiconductor transition in germanium. Phys. Rev. B Condens. Matter *49*, 14251–14269. https://doi.org/10.1103/PhysRevB.49.14251.

73. Kresse, G., and Furthmüller, J. (1996). Efficiency of ab-initio total energy calculations for metals and semiconductors using a plane-wave basis set. Comput. Mater. Sci. *6*, 15–50. https://doi.org/10.1016/0927-0256(96)00008-0.

74. Kresse, G., and Furthmüller, J. (1996). Efficient iterative schemes for ab initio total-energy calculations using a plane-wave basis set. Phys. Rev. B Condens. Matter *54*, 11169–11186. https://doi.org/10.1103/PhysRevB.54.11169.

75. Blöchl, P.E. (1994). Projector augmented-wave method. Phys. Rev. B Condens. Matter *50*, 17953–17979. https://doi.org/10.1103/PhysRevB.50.17953.

76. Kresse, G., and Joubert, D. (1999). From ultrasoft pseudopotentials to the projector augmented-wave method. Phys. Rev. B *59*, 1758–1775. https://doi.org/10.1103/PhysRevB.59.1758.

77. Perdew, J.P., Burke, K., and Ernzerhof, M. (1996). Generalized Gradient Approximation Made Simple. Phys. Rev. Lett. *77*, 3865–3868. https://doi.org/10.1103/PhysRevLett.77.3865.

78. Monkhorst, H.J., and Pack, J.D. (1976). Special points for Brillouin-zone integrations. Phys. Rev. B *13*, 5188–5192. https://doi.org/10.1103/PhysRevB.13.5188.

79. Grimme, S., Antony, J., Ehrlich, S., and Krieg, H. (2010). A consistent and accurate ab initio parametrization of density functional dispersion correction (DFT-D) for the 94 elements H-Pu. J. Chem. Phys. *132*, 154104. https://doi.org/10.1063/1.3382344.

80. Yang, J., Kim, M., Lee, S., Yoon, J.W., Shome, S., Bertens, K., Song, H., Lim, S.G., Oh, J.T., Bae, S.Y., et al. (2021). Solvent Engineering of Colloidal Quantum Dot Inks for Scalable Fabrication of Photovoltaics. ACS Appl. Mater. Interfaces *13*, 36992–37003. https://doi.org/10.1021/acsami.1c06352.

81. Oh, J.T., Bae, S.Y., Yang, J., Ha, S.R., Song, H., Lee, C.B., Shome, S., Biswas, S., Lee, H.-M., Seo, Y.-H., et al. (2021). Ultra-stable all-inorganic silver bismuth sulfide colloidal nanocrystal photovoltaics using pin type architecture. J. Power Sources *514*, 230585. https://doi.org/10.1016/j.jpowsour.2021.230585.

82. Han, Q., Bae, S.-H., Sun, P., Hsieh, Y.-T., Yang, Y.M., Rim, Y.S., Zhao, H., Chen, Q., Shi, W., Li, G., et al. (2016). Single Crystal Formamidinium Lead Iodide (FAPbI3): Insight into the Structural, Optical, and Electrical Properties. Adv. Mater. *28*, 2253–2258. https://doi.org/10.1002/adma.201505002.